

# T-Phase and H-Phase Coupled TMD van der Waals Heterostructure ZrS<sub>2</sub>/MoTe<sub>2</sub> with Both Rashba Spin Splitting and Type-III Band Alignment

Xiujuan Mao, Jia Li,\* Ze Liu, Guang Wang, Qian Zhang, and Yuming Jin



Cite This: *J. Phys. Chem. C* 2022, 126, 10601–10609



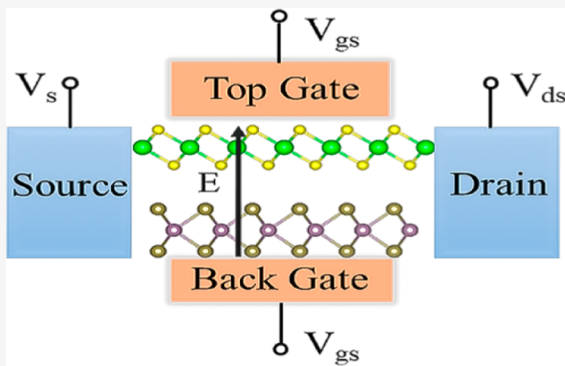
Read Online

ACCESS |

Metrics & More

Article Recommendations

**ABSTRACT:** Based on first-principles calculations, we systematically explored the electronic structures of the ZrS<sub>2</sub>/MoTe<sub>2</sub> heterostructure. The results show that Rashba splitting and type-III band alignment coexist in this heterostructure system. The presence of Rashba spin splitting makes this system of interest for spin-field-effect transistor applications. The effects of biaxial strain and an applied electric field on the electronic structure of a heterostructure were also explored. In the strain range of -2 to 6%, the system keeps the structural stability, and the electronic structure maintains the type-III band alignment. In particular, a crucial change from a type-III to a type-II band alignment occurred under the negative electric field of -0.4 to -0.6 V/Å, which can be beneficial to design multi-purpose devices. The current work predicts that the ZrS<sub>2</sub>/MoTe<sub>2</sub> heterostructure is an excellent candidate for the realization of multiple band arrangement conversion and tunnel-field-effect transistors, which deserves further experimental research.



## 1. INTRODUCTION

Van der Waals heterostructures based on transition-metal dichalcogenides (TMDs) have attracted extensive research interest because of their flexible ability to integrate highly diverse two-dimensional (2D) materials at the atomic scale, thus providing a compelling platform for a variety of electrons and photoelectrons.<sup>1–3</sup> According to the traditional band arrangement, van der Waals heterostructures can be divided into three types, that is, straddling type-I, staggered type-II, and broken-gap type-III.<sup>4</sup> Most heterostructures show a type-I or a type-II band alignment, but it has been shown that few systems belong to the type-III band alignment.<sup>5–7</sup> Due to the quantum tunneling mechanism, the type-III heterostructure is widely used in various high-speed and low-power devices, and this band arrangement is also essential for tunnel devices, for example, negative differential resistance.<sup>8,9</sup> It was reported that a broken-gap van der Waals heterostructure PtS<sub>2</sub>/WSe<sub>2</sub> exhibits an ultrahigh reverse rectification ratio, on/off ratio room temperature, and excellent photodetection properties.<sup>10</sup> Under biaxial strain and an external electric field, the MoS<sub>2</sub>/C<sub>3</sub>N van der Waals heterostructure still maintains the character of a broken-gap and the type-III alignment.<sup>11</sup> The large biaxial strain and applied electric field are required to realize the transition from type II to type III in MoS<sub>2</sub>/WSe<sub>2</sub> and GeC/WS<sub>2</sub> heterostructures, respectively.<sup>12,13</sup> In addition, the Rashba effect plays a decisive role in the electronic states of heterostructures and surfaces because the structural asymmetry

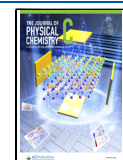
causes an out-of-plane electric field. Datta and Das first proposed tunneling field-effect transistors based on Rashba spin splitting in 1990.<sup>14</sup> Based on this, many design schemes have been proposed, for example, single- and double-diamond devices, made of materials with strong spin-orbit coupling (SOC), can act as both a spin filter and a spin analyzer.<sup>15–17</sup> Therefore, a natural question could be raised whether the type-III band arrangement and Rashba spin splitting can coexist in a material. To our knowledge, the reports about that are very rare.

Due to their special physical and chemical properties and potential applications in electronic and optoelectronic devices, TMDs have stimulated great research enthusiasm. The T-phase ZrS<sub>2</sub> monolayer was successfully synthesized experimentally, which is suitable for thermoelectric, photocatalytic water splitting, and photovoltaic applications.<sup>18</sup> However, the spin degeneracy in ZrS<sub>2</sub> is protected by inversion symmetry, which impedes its application in tunneling field-effect transistors.<sup>19,20</sup> To improve the degeneracy, the structural inversion asymmetry should be introduced, such as through

Received: April 26, 2022

Revised: May 30, 2022

Published: June 21, 2022



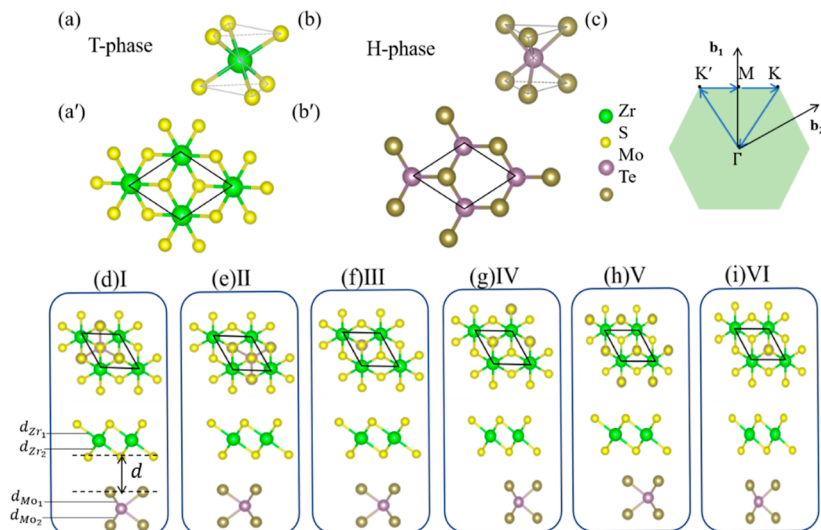


**Figure 1.** (a) T- and (b) H-phase structures in layered TMDs. Crystal structure of (a') T-phase ZrS<sub>2</sub> and (b') H-phase MoTe<sub>2</sub>. (c) Brillouin zone of the hexagonal structure with markings of the high-symmetry points. (d–i) Top views of the six configurations I–VI of the ZrS<sub>2</sub>/MoTe<sub>2</sub> heterostructure. The green, yellow, purple, and brown spheres represent the Zr, S, Mo, and Te atoms, respectively. The black frame indicates the range of the unit cell.

doping,<sup>21,22</sup> defects,<sup>23,24</sup> and surface functionalization.<sup>25,26</sup> Among these strategies, the construction of heterostructures is considered to be a general platform for device applications.<sup>27,28</sup> In addition, the H-phase TMDs do not have space inversion symmetry, for example, for MoTe<sub>2</sub>, the Mo and Te atoms occupy one of two inequivalent triangular sublattices, respectively. Also, the monolayer H-phase MoTe<sub>2</sub> has a strong SOC, which splits the valence band by  $\sim 250$  meV as compared to the  $\sim 150$  meV of MoS<sub>2</sub>.<sup>29–31</sup> Therefore, the heterostructure composed of T-phase and H-phase TMD monolayers possesses a broken inversion symmetry, which provides a promising platform for the study of spin physics.

In this work, we studied the 2D ZrS<sub>2</sub>/MoTe<sub>2</sub> heterostructures including T-phase ZrS<sub>2</sub> and H-phase MoTe<sub>2</sub>. As both ZrS<sub>2</sub> and MoTe<sub>2</sub> are standard 2D semiconducting TMDCs with high mobility<sup>32</sup> and have been extensively studied,<sup>33,34</sup> the ZrS<sub>2</sub>/MoTe<sub>2</sub> heterostructure has high experimental feasibility. Using first-principles calculations, we systematically investigate the electronic properties of the ZrS<sub>2</sub>/MoTe<sub>2</sub> heterostructure. The results show that it has two characteristics simultaneously, that is, a type-III band arrangement and Rashba spin splitting. These characteristics make its application in field-effect transistors very favorable. The energy and dynamic stability of the heterostructure are also confirmed. In addition, we also used strain and an electric field to tune the electronic properties of the ZrS<sub>2</sub>/MoTe<sub>2</sub> heterostructure, and it was found that the electronic properties were sensitive to biaxial strain and electric fields. Importantly, type-II band alignments can be induced by applying an external electric field, which indicates that multi-purpose devices can be designed.

## 2. COMPUTATIONAL DETAILS

All the density functional theory calculations were performed by using the Vienna ab initio simulation package.<sup>35,36</sup> The interaction between the core and valence electrons was described using the projected augmented wave potential. The Perdew–Burke–Ernzerhof functional was used to describe the exchange and correlation interactions.<sup>37,38</sup> An energy cutoff of

450 eV was used to expand the plane wave, and van der Waals interactions were considered using the DFT-D2 method.<sup>39</sup> The Brillouin zone was integrated using a Monkhorst–Pack mesh of  $20 \times 20 \times 1$   $k$ -points for the structural relaxation of the unit cell of MoTe<sub>2</sub>, ZrS<sub>2</sub>, and the ZrS<sub>2</sub>/MoTe<sub>2</sub> heterostructures. Also,  $30 \times 30 \times 1$   $k$ -points were used for the band structure calculation of MoTe<sub>2</sub>, ZrS<sub>2</sub>, and the ZrS<sub>2</sub>/MoTe<sub>2</sub> heterostructures. To avoid the interaction between image atoms, the vacuum spacing of 20 Å was added on the surface of the monolayers and heterostructures. Structural relaxation was performed using the conjugate-gradient algorithm until the total energy converged to  $10^{-4}$  eV and the Hellmann–Feynman force on each atom was less than 0.02 eV/Å.

## 3. RESULTS AND DISCUSSION

### 3.1. Structural Properties of the ZrS<sub>2</sub>/MoTe<sub>2</sub> Heterostructure.

From the perspective of structure, the 2D TMDs can be categorized as the octahedral (tetragonal, T) phase and the trigonal prismatic (hexagonal, H) phase as shown in Figure 1a,b. The T-phase has a triangular chalcogenide element at the top of the monolayer, and a 180° rotation structure at the bottom can also be called a triangular antiprism structure, resulting in hexagonal atoms in the top view (Figure 1a). In the H-phase material, each metal atom extends six branches in the  $z$  direction and downward to form two tetrahedrons, and the hexagonal symmetry can be seen in the top view (Figure 1b). The T-phase ZrS<sub>2</sub> monolayer is a hexagonal lattice with two S atoms and one Zr atom per unit cell. The calculated lattice parameter of monolayer ZrS<sub>2</sub> is 3.68 Å, which is very consistent with the experimental and theoretical value of about 3.69 Å reported previously.<sup>40,41</sup> Herein, we use a monolayer H-phase MoTe<sub>2</sub>, which can be fabricated from the corresponding H-phase bulk material with a honeycomb hexagonal lattice structure by mechanical exfoliation, and its lattice constant is 3.56 Å.<sup>42,43</sup> In addition, the crystal structures of ZrS<sub>2</sub> and MoTe<sub>2</sub> are shown in Figure 1a',b', respectively. The ZrS<sub>2</sub>/MoTe<sub>2</sub> heterostructure has a lattice mismatch of 3.3%. We use  $1 \times 1$  ZrS<sub>2</sub> and  $1 \times 1$  MoTe<sub>2</sub> primitive cells to

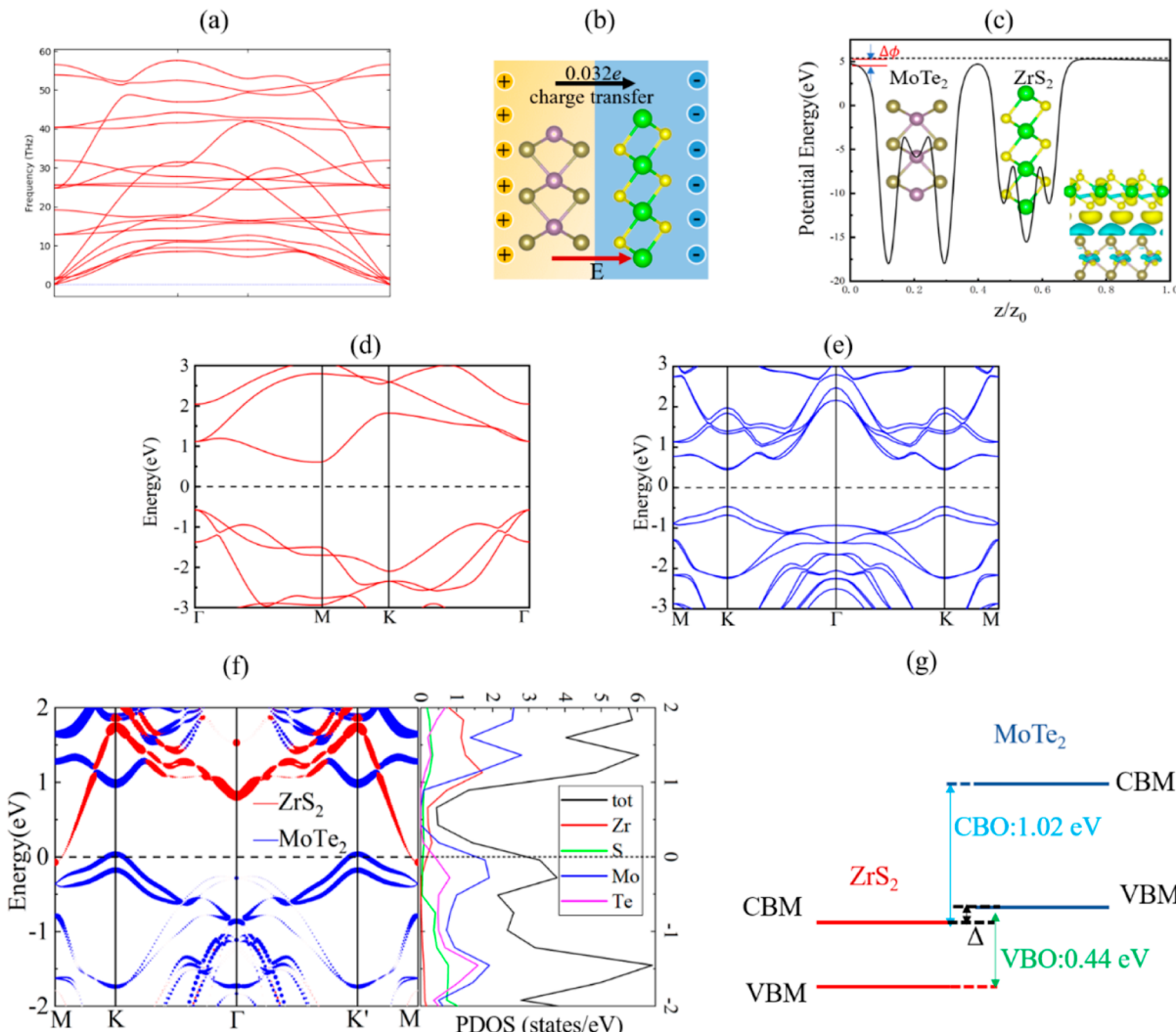


**Figure 2.** (a) Calculated phonon band structure for configuration I. (b) Schematic diagram of the charge transfer for the ZrS<sub>2</sub>/MoTe<sub>2</sub> heterostructure calculated by Bader charge analysis. The number indicates the amount of charge transfer. The black and red arrows indicate the direction of charge transfer and the electric field at the interface, respectively. The “+” and “−” denote the positive and negative electricity, respectively. (c) Planar average of the electrostatic potential energy of the ZrS<sub>2</sub>/MoTe<sub>2</sub> heterostructure, in which  $z$  is the coordinate variable in the vertical direction,  $z_0$  is the thickness of the unit cell, and  $z/z_0$  refers to the relative position in the vertical direction.  $\Delta\phi$  is the work function difference. Band structures of (d) monolayer ZrS<sub>2</sub> and (e) monolayer MoTe<sub>2</sub> with SOC. (f) Projected band structure and PDOS of the ZrS<sub>2</sub>/MoTe<sub>2</sub> heterostructure with SOC. The red and blue lines show the ZrS<sub>2</sub> and MoTe<sub>2</sub> components of the ZrS<sub>2</sub>/MoTe<sub>2</sub> heterostructure, respectively. The Fermi level is set to zero and indicated by the black dashed line. (g) Band alignment of the ZrS<sub>2</sub>/MoTe<sub>2</sub> heterostructure.

construct the ZrS<sub>2</sub>/MoTe<sub>2</sub> heterostructure. For the in-plane lattice constant of the heterostructure, we use the average value 3.62 Å of ZrS<sub>2</sub> (3.68 Å) and MoTe<sub>2</sub> (3.56 Å). We investigated six possible configurations of the ZrS<sub>2</sub>/MoTe<sub>2</sub> heterostructure, named configurations I–VI, as shown in Figure 1d–i, respectively. We defined  $d$  as the distance between the lower layer S atoms and the higher Te atoms. The Brillouin zone with high symmetry points and the  $k$ -path used for presenting the band structures are shown in Figure 1c.

The most energy-favorable stacking of the ZrS<sub>2</sub>/MoTe<sub>2</sub> heterostructure was evaluated by calculating the binding energy ( $\Delta_E$ ), which is expressed as the formula<sup>44</sup>

$$\Delta_E = E_{\text{ZrS}_2/\text{MoTe}_2} - E_{\text{ZrS}_2} - E_{\text{MoTe}_2} \quad (1)$$

where  $E_{\text{ZrS}_2/\text{MoTe}_2}$ ,  $E_{\text{ZrS}_2}$ , and  $E_{\text{MoTe}_2}$  are the total energy of the ZrS<sub>2</sub>/MoTe<sub>2</sub> heterostructure and isolated monolayers ZrS<sub>2</sub> and MoTe<sub>2</sub>, respectively. The calculation results of six config-

urations show that the most stable structure is configuration I ( $-0.059$  eV), and the equilibrium distance between ZrS<sub>2</sub> and MoTe<sub>2</sub> is 2.75 Å. The phonon band structure of configuration I is shown in Figure 2a, and there exists no imaginary frequency, indicating its dynamic stability. Figure 2b shows the charge transfer of the ZrS<sub>2</sub>/MoTe<sub>2</sub> heterostructure calculated by Bader charge analysis. With different electronegativity values of Zr ( $-1.996$ ), S ( $+2.028$ ), Mo ( $-0.489$ ), and Te ( $+0.457$ ), where the positive and negative signs represent the gain and loss of electrons, respectively, we find that the charge transfer has occurred from the MoTe<sub>2</sub> to the ZrS<sub>2</sub> layer, and the amount of transferred charge is 0.032 e. We also calculated the charge density difference to further investigate its binding character, which is expressed as

$$\Delta\rho = \rho_{\text{ZrS}_2/\text{MoTe}_2} - \rho_{\text{ZrS}_2} - \rho_{\text{MoTe}_2} \quad (2)$$

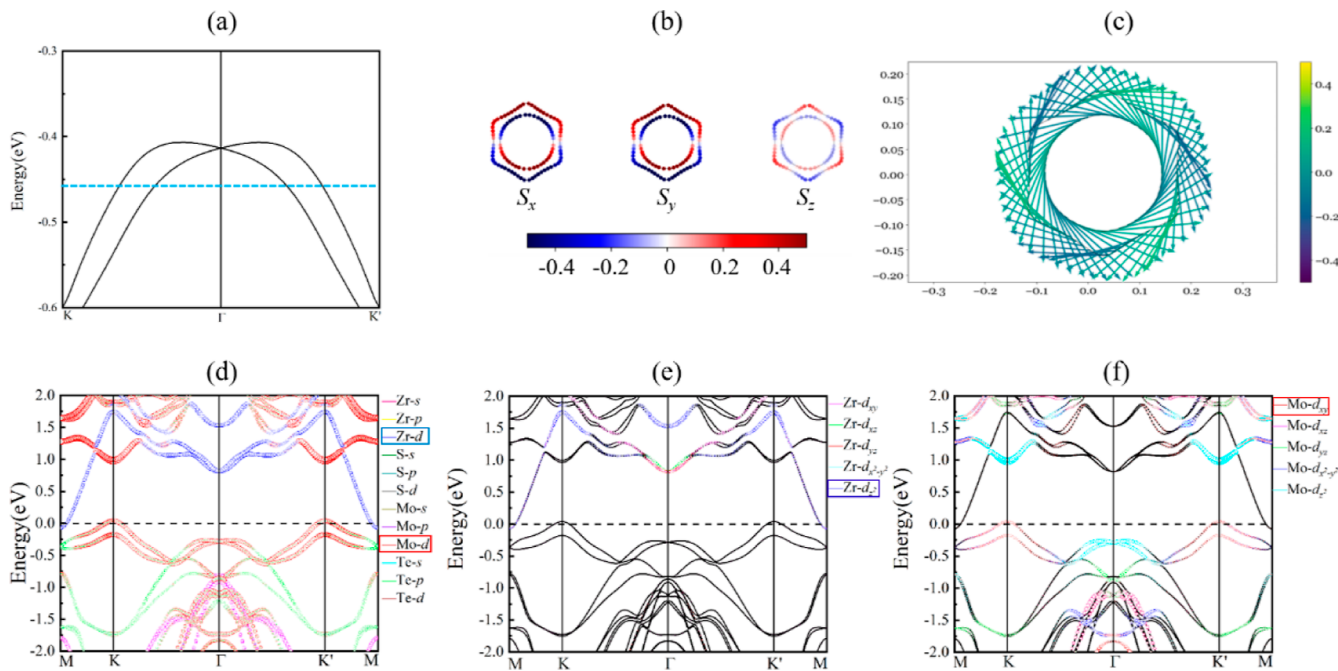


**Figure 3.** (a) Magnified electronic structure of the  $\text{ZrS}_2/\text{MoTe}_2$  heterostructure near the  $\Gamma$  point. (b) Spin polarization components around the  $\Gamma$  point for a constant energy cutoff [blue dotted line in (a)]. Arrows indicate the spin direction, while their color indicates the degree of spin polarization. The scale bars in (b) represent spin polarization. (d–f) Orbital-projected band structures of the  $\text{ZrS}_2/\text{MoTe}_2$  heterostructure. The radius of each circle is proportional to the magnitude of the orbital contributions.

where  $\rho_{\text{ZrS}_2/\text{MoTe}_2}$ ,  $\rho_{\text{ZrS}_2}$ , and  $\rho_{\text{MoTe}_2}$  are the charge densities of the heterostructure system and isolated monolayers  $\text{ZrS}_2$  and  $\text{MoTe}_2$ , respectively. The charge density difference of the  $\text{ZrS}_2/\text{MoTe}_2$  heterostructure is shown in the right inset of Figure 2c. It can be seen that the charges are redistributed in the interface region, accumulated near the  $\text{ZrS}_2$  layer, and depleted close to the  $\text{MoTe}_2$  layer. The greater electron accumulation on the monolayer  $\text{ZrS}_2$  side leads to the larger potential energy and work function than that of the monolayer  $\text{MoTe}_2$  side as shown in Figure 2c. Hence, the Fermi level of  $\text{MoTe}_2$  is higher than that of  $\text{ZrS}_2$ . When forming a heterostructure, the electrons transfer from  $\text{MoTe}_2$  to  $\text{ZrS}_2$  until the Fermi level is balanced, resulting in an interfacial electric field pointing from  $\text{MoTe}_2$  to  $\text{ZrS}_2$ , as shown by the red arrow in Figure 2b. Because the work function difference is independent of any reference surface, we give the value of the work function difference ( $\Delta\phi$ ), 0.577 eV, in the  $\text{ZrS}_2/\text{MoTe}_2$  heterostructure. The work function difference can drive the spontaneous movement of interfacial electrons or holes, further resulting in an interfacial electric field.

**3.2. Electronic Properties of the  $\text{WSe}_2/\text{FeCl}_2$  Heterostructure.** Figure 2d,e shows the band structures with SOC of the monolayers  $\text{ZrS}_2$  and  $\text{MoTe}_2$ .  $\text{ZrS}_2$  has an indirect band gap of 1.19 eV<sup>38</sup> and  $\text{MoTe}_2$  has a direct band gap of 1.1 eV, which is consistent with previous reports.<sup>37</sup> When SOC is considered, the  $\text{ZrS}_2/\text{MoTe}_2$  heterostructure shows a type-III band alignment (broken-gap) because the valence band maximum (VBM) of  $\text{MoTe}_2$  is higher than the conduction band minimum (CBM) of  $\text{ZrS}_2$ , as shown in Figure 2f. In addition, it can be seen from the partial density of states (PDOS) (Figure 2f) that the CBM and VBM of the heterostructure pass through the Fermi level. In other words, there is no overlap of the band gaps for  $\text{MoTe}_2$  and  $\text{ZrS}_2$  monolayers in the heterostructure, indicating that the  $\text{ZrS}_2/\text{MoTe}_2$  heterostruc-

ture has a type-III band alignment, which is schematically shown in Figure 2g. The conduction band offset (CBO) and valence band offset (VBO) are 1.02 and 0.44 eV, respectively, and the band overlap  $\Delta$  ( $\Delta = E_{\text{MoTe}_2}^{\text{VBM}} - E_{\text{ZrS}_2}^{\text{CBM}}$ ) is 0.111 eV for the  $\text{ZrS}_2/\text{MoTe}_2$  heterostructure. This structure is quite favorable for applications in tunneling devices.

From the vicinity of the  $\Gamma$  point in Figure 2f, we can see that the Rashba splitting is very similar to that in heavy metal surfaces and semiconductor quantum wells.<sup>45–48</sup> The Rashba type spin splitting exists in the structure-reversal symmetry breaking the  $\text{ZrS}_2/\text{MoTe}_2$  heterostructure, in which the energy bands of the two spin directions are shifted along the momentum direction. The calculated spin polarization components  $S_x$ ,  $S_y$ , and  $S_z$  at a constant energy cutoff, as indicated by the blue dotted horizontal line in Figure 3a, are shown in Figure 3b. The arrows show the in-plane orientation of the spin, and their color indicates the degree of spin polarization (Figure 3c). The spin direction is mainly in the  $x$ – $y$  plane; the arrows show outer and inner circles with clockwise and counterclockwise rotating spin directions, respectively. Both the inner circle and outer open contours around  $\Gamma$  exhibit a helical spin structure, corresponding to the two Rashba spin splitting bands. To elucidate the origin of the orbital at the CBM and VBM, we calculated the orbital-projection of atoms, and the results are provided in Figure 3d–f. The figure shows that the CBM is mainly contributed by the  $\text{Zr}-d_z^2$  orbitals of  $\text{ZrS}_2$ , and the VBM is mainly contributed by  $\text{Mo}-d_x-d_z$  orbitals of  $\text{MoTe}_2$ . The observed Rashba bands around the  $\Gamma$  point in the  $\text{ZrS}_2/\text{MoTe}_2$  heterostructure are  $\text{Mo}-d_z^2$  state orbitals of  $\text{MoTe}_2$ .

The strains within the suitable range from a −6% compressive strain to a 6% tensile strain were applied in the biaxial direction to explore the strain effect on the electronic structure and dynamic stability. The band structures of the

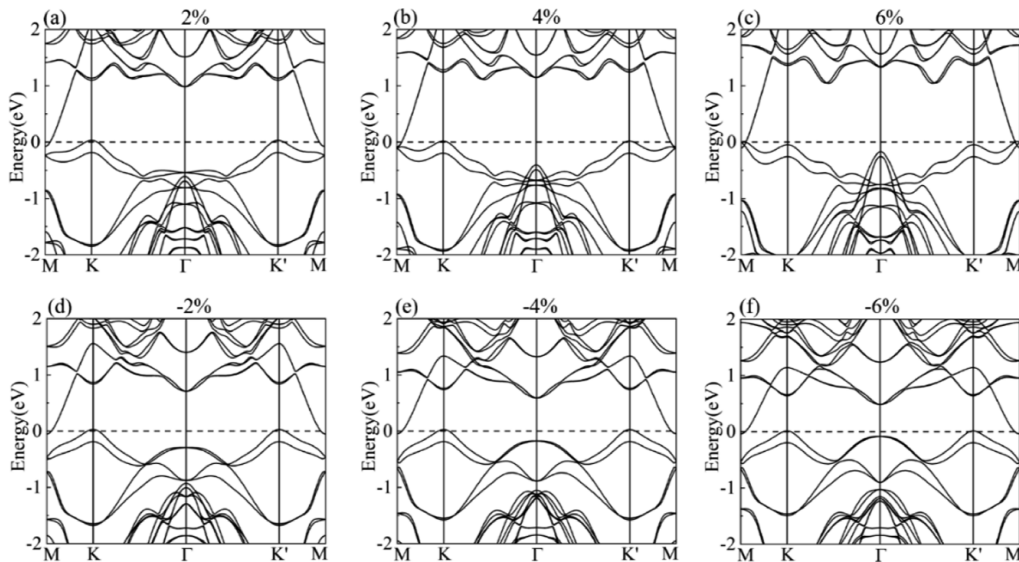


**Figure 4.** (a–f) Band structures of the  $\text{ZrS}_2/\text{MoTe}_2$  heterostructure under  $\pm 2$ ,  $\pm 4$ , and  $\pm 6\%$  strains. The Fermi level is indicated by the dashed line.

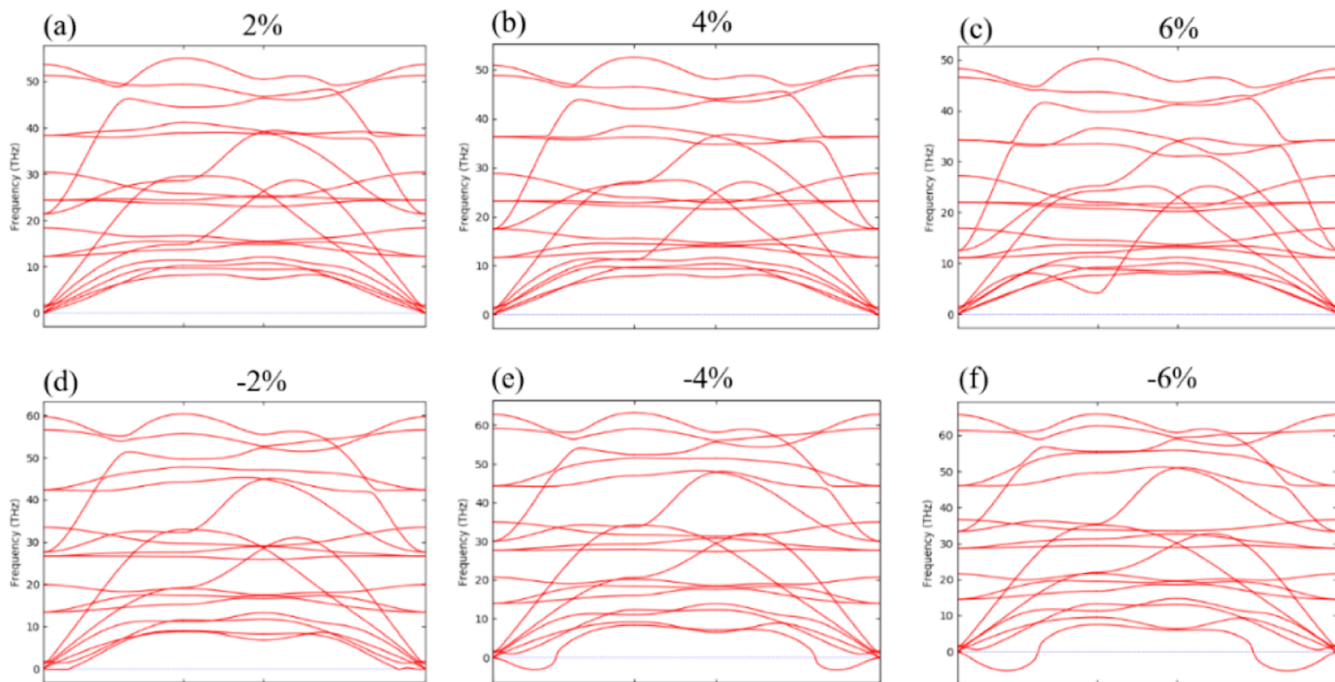


**Figure 5.** (a–f) Phonon band structures of the  $\text{ZrS}_2/\text{MoTe}_2$  heterostructure under  $\pm 2$ ,  $\pm 4$ , and  $\pm 6\%$  strains.

$\text{ZrS}_2/\text{MoTe}_2$  heterostructure under various biaxial strains are shown in Figure 4a–f, and the corresponding phonon spectra are shown in Figure 5a–f. It can be seen from Figure 5 that the heterostructure under the strain range of  $-2$  to  $6\%$  is dynamically stable because there is no virtual frequency. In the strain range of  $-2$  to  $4\%$ , the VBM and CBM of the electronic band are located at the  $K$  ( $K'$ ) point and the  $M$  point, respectively. When the strain reaches  $6\%$ , the VBM moves from the  $K$  ( $K'$ ) to the  $M$  point, and the CBM remains at the  $M$  point. We note that in the whole strain range, the band structure maintains the type-III alignment. This reveals that the  $\text{ZrS}_2/\text{MoTe}_2$  heterostructure is quite favorable for applications in tunneling devices based on the broken-gap heterostructures.

The application of an external electric field is widely used not only in theory but also in experiments to tune the electronic structure of 2D materials.<sup>49–51</sup> The effect of the external electric field on the electronic properties of the  $\text{ZrS}_2/\text{MoTe}_2$  heterostructure was investigated. Here, the direction of the positive electric field is designated as pointing from the  $\text{ZrS}_2$  layer to the  $\text{MoTe}_2$  layer. The band structures of the  $\text{ZrS}_2/\text{MoTe}_2$  heterostructure under various electric fields are shown in Figure 6a–f, and the corresponding phonon spectra are shown in Figure 7a–f. It can be seen from Figure 7 that the heterostructure under the strain range of  $-0.6$  to  $0.6 \text{ V}/\text{\AA}$  is dynamically stable because there is no virtual frequency. It is clearly shown that the band gaps of the heterostructure are highly sensitive to the external electric field. Under the electric

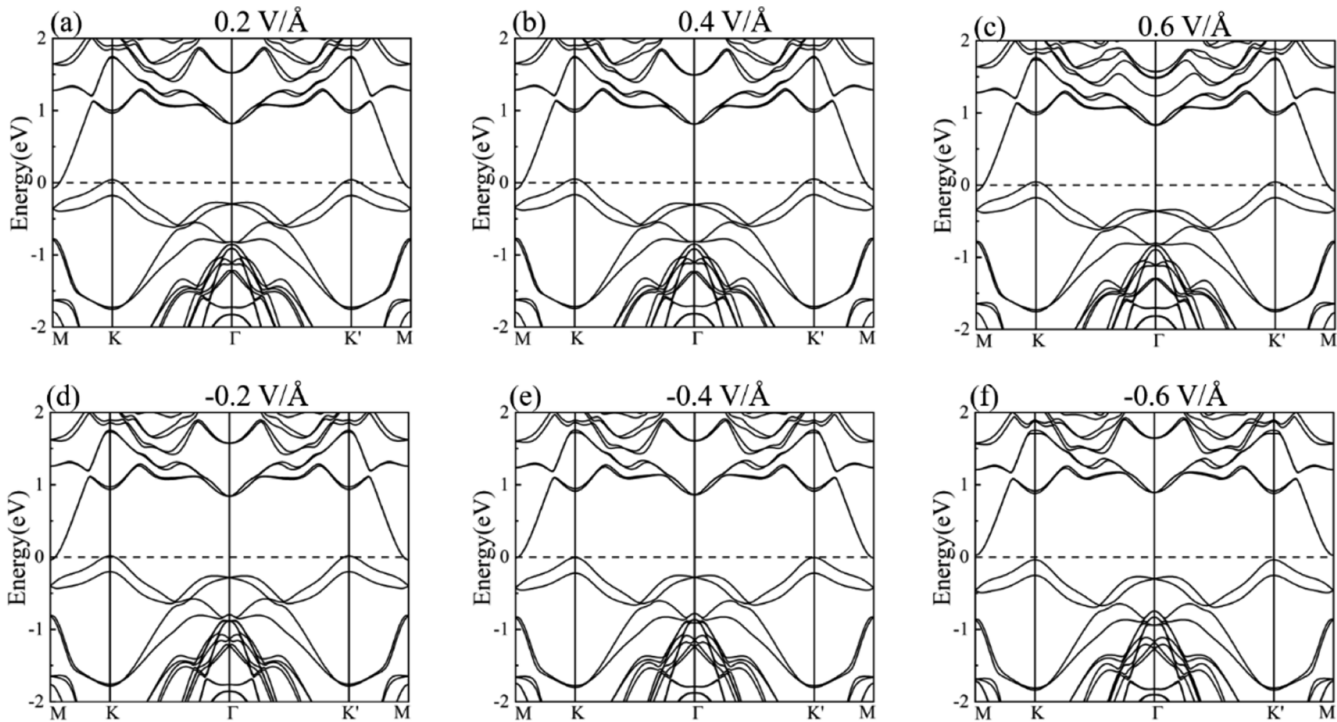


**Figure 6.** (a–f) Band structures of the  $\text{ZrS}_2/\text{MoTe}_2$  heterostructure at various values of electric fields:  $\pm 0.2$ ,  $\pm 0.4$ , and  $\pm 0.6 \text{ V}/\text{\AA}$ , respectively.

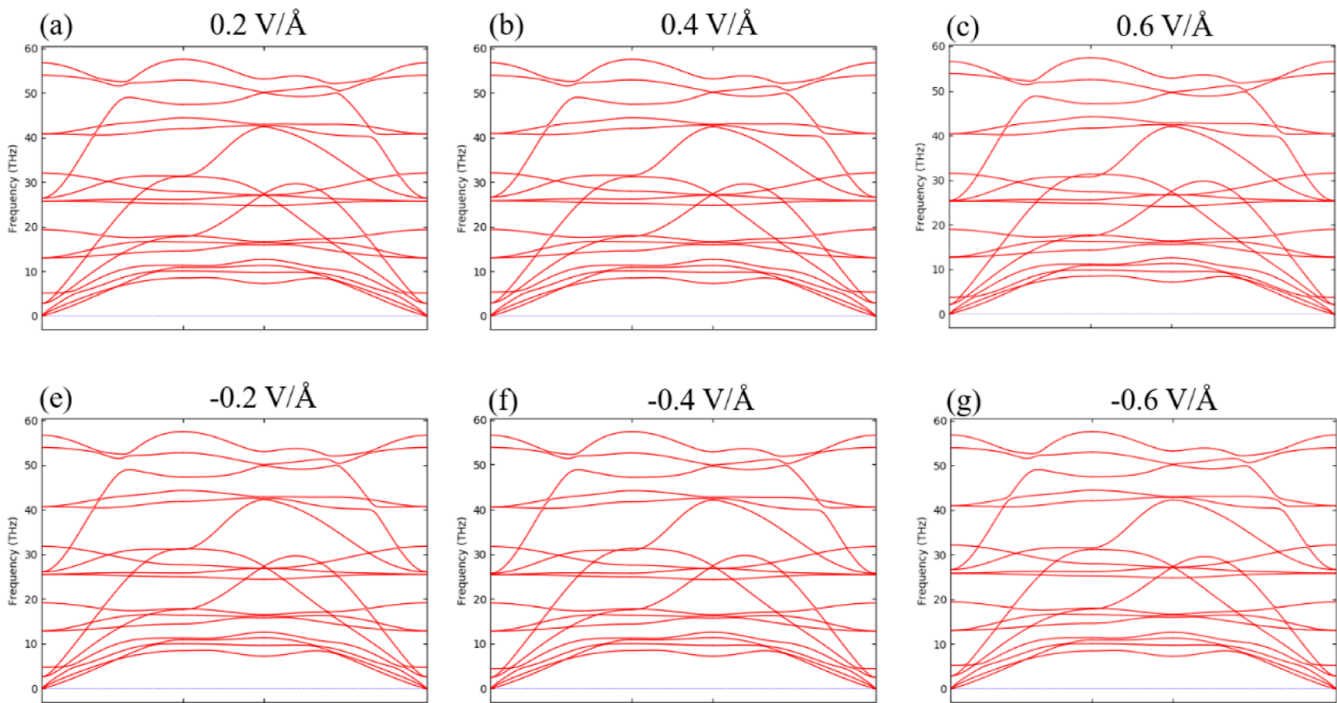


**Figure 7.** (a–f) Phonon band structure of the  $\text{ZrS}_2/\text{MoTe}_2$  heterostructure at various values of electric fields:  $\pm 0.2$ ,  $\pm 0.4$ , and  $\pm 0.6 \text{ V}/\text{\AA}$ , respectively.

field from  $-0.2$  to  $0.6 \text{ V}/\text{\AA}$ , the  $\text{ZrS}_2/\text{MoTe}_2$  heterostructure preserves the type-III band alignment. In Figure 6e, when the applied negative electric field is  $-0.4 \text{ V}/\text{\AA}$ , the band edge of the  $\text{MoTe}_2$  layer is pushed down, but the band edge of the  $\text{ZrS}_2$  layer is pulled up, thus inducing an interesting transition from a type-III to a type-II band arrangement in the  $\text{ZrS}_2/\text{MoTe}_2$  heterostructure, with a band gap of  $0.005 \text{ eV}$ . As shown in Figure 6f, when the negative electric field further increases

to  $-0.6 \text{ V}/\text{\AA}$ , the heterostructure maintains the type-II arrangement, and the band gap increases to  $0.062 \text{ eV}$ . The variations of bond lengths (see Figure 1d) under the external electric field of  $-0.6$ – $0.6 \text{ V}/\text{\AA}$  are shown in Figure 8. As shown in Figure 1d, the bond lengths  $d_{\text{Zr}_1}(d_{\text{Zr}_2})$  is defined as the distance between Zr and the upper (lower) layer S, and  $d_{\text{Mo}_1}(d_{\text{Mo}_2})$  is defined as the distance between Mo and the upper(lower) layer Te. In the electric field range of  $-0.6$  to  $0$

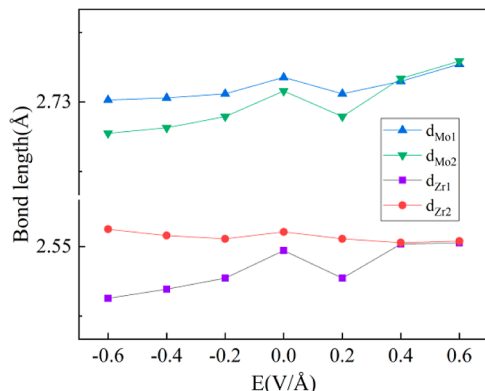


**Figure 8.** Variation of the bond length  $d_{\text{Mo}_1}$ ,  $d_{\text{Mo}_2}$ ,  $d_{\text{Zr}_1}$  and  $d_{\text{Zr}_2}$  under the electric field of  $-0.6$ – $0.6$  V/Å.

V/Å, the bond lengths of  $d_{\text{Mo}_1}$ ,  $d_{\text{Mo}_2}$ , and  $d_{\text{Zr}_1}$  increase, while the bond length of  $d_{\text{Zr}_2}$  decreases. In the electric field range of 0–2 V/Å, the bond lengths of  $d_{\text{Mo}_1}$ ,  $d_{\text{Mo}_2}$ ,  $d_{\text{Zr}_1}$ , and  $d_{\text{Zr}_2}$  decrease until the electric field increases to 4 V/Å. For the range of 0.4–0.6 V/Å, the bond lengths of  $d_{\text{Mo}_1}$  ( $d_{\text{Zr}_1}$ ) approach  $d_{\text{Mo}_2}$  ( $d_{\text{Zr}_2}$ ). The variation of the bond lengths under the electric field will affect the configuration of electrons as well as the corresponding orbital hybridization, and then the coupling interaction between transition-metal atoms will change accordingly.

The band overlap, band alignment, and band gap under the external electric field of  $-0.6$ – $0.6$  V/Å are given in **Table 1**.

**Table 1.** Band Overlap  $\Delta$  (eV), Band Alignment (Type), and Band Gap (eV) under the Electric Field of  $-0.6$ – $0.6$  V/Å

electric field (V/Å)							
	-0.6	-0.4	-0.2	0	0.2	0.4	0.6
$\Delta$			0.052	0.11	0.114	0.140	0.124
type	II	II	III	III	III	III	III
gap (eV)	0.062	0.005					

Within the range of  $-0.2$  to  $0.6$  V/Å, the system maintains the type-III band arrangement, and the band overlap ranges from 0.052 to 0.124 eV. The electric field of  $-0.2$  V/Å leads to the minimum band overlap 0.052 eV, very close to zero, and then the corresponding probability of tunneling is the maximum. As the electric field changes from  $-0.4$  to  $-0.6$  V/Å, the system changes to the type-II band arrangement with the band gap of 0.005 eV for  $-0.4$  V/Å and 0.062 eV for  $-0.6$  V/Å. The response of electronic characteristics to various electric fields is very crucial to designing novel electronic devices.

Based on the above results, we proposed a multiple-purpose device prototype based on the  $\text{ZrS}_2/\text{MoTe}_2$  heterostructure, which is shown in **Figure 9**. The device consists of a source, a drain, a channel, and two gates for introducing the external electric field. The source and drain of the device are ferromagnetic materials with the same spin orientation along the  $+z$  direction. When the spin electrons are injected from the source and transmitted in the channel along the  $z$  direction, Rashba spin splitting can produce an effective magnetic field in the plane, and the spin generates precession in this effective magnetic field. When the spin direction of the electron reaching the drain is opposite to that of the source electron,

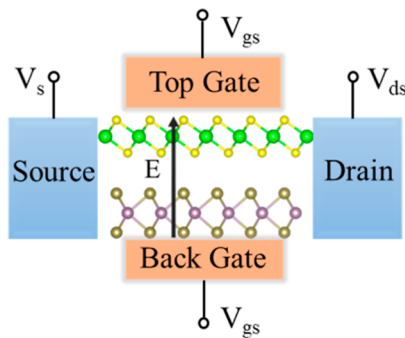


**Figure 9.** Schematic diagram of a multiple-purpose device based on the  $\text{ZrS}_2/\text{MoTe}_2$  heterostructure.

the electron is repelled by the drain to be non-conductive, and this can be regarded as a closed state. The electron can pass through the drain when the electronic spin direction of the drain is the same as the source, and this is an on state. Therefore, the spin orientation can be controlled by the electric field and acts as a switch. By changing the magnitude and direction of the gate voltage, different band alignments can be obtained. Type-III band alignment can be used for tunnel field-effect transistors, and type-II band alignment can be used for unipolar electronic applications. This multifunctional device is worthy of further experimental research.

#### 4. CONCLUSIONS

In summary, through first-principles calculations, we demonstrate that the  $\text{ZrS}_2/\text{MoTe}_2$  heterostructure exhibits a remarkable type-III band alignment and Rashba spin splitting. We also find that applying biaxial strain and an electric field can effectively regulate the electronic properties of  $\text{ZrS}_2/\text{MoTe}_2$  heterostructures. Under the strain range of  $-2$ – $6$ %, the system keeps the structural stability, and the electronic structure maintains the type-III band alignment. The above results indicate that the  $\text{ZrS}_2/\text{MoTe}_2$  heterostructure is quite favorable for applications in tunneling devices. Moreover, a crucial transition from type-III to type-II band alignments was observed in the  $\text{ZrS}_2/\text{MoTe}_2$  heterostructure under the applied electric field. These studies provide theoretical knowledge about the  $\text{ZrS}_2/\text{MoTe}_2$  heterostructure and give guidance for possible applications in the tunnel field-effect transistors as well as multiple-purpose electronic devices.

#### ■ AUTHOR INFORMATION

##### Corresponding Author

Jia Li – School of Materials Science and Engineering and School of Science, Hebei University of Technology, Tianjin 300401, People's Republic of China; [ORCID iD: 0000-0002-8594-8356](https://orcid.org/0000-0002-8594-8356); Phone: +86 22 60435638; Email: [jiali@hebut.edu.cn](mailto:jiali@hebut.edu.cn); Fax: +86 22 60435639

##### Authors

Xiujuan Mao – School of Materials Science and Engineering, Hebei University of Technology, Tianjin 300401, People's Republic of China

Ze Liu – School of Materials Science and Engineering, Hebei University of Technology, Tianjin 300401, People's Republic of China

Guang Wang – School of Science, Hebei University of Technology, Tianjin 300401, People's Republic of China

Qian Zhang – School of Science, Hebei University of Technology, Tianjin 300401, People's Republic of China  
Yuming Jin – School of Science, Hebei University of Technology, Tianjin 300401, People's Republic of China

Complete contact information is available at:

<https://pubs.acs.org/10.1021/acs.jpcc.2c02891>

## Notes

The authors declare no competing financial interest.

## ACKNOWLEDGMENTS

We would like to acknowledge the support by the National Natural Science Foundation of China (grant no. 61671199) and the Natural Science Foundation of Hebei Province (grant no. A2020202010).

## REFERENCES

- (1) Gan, K.-J.; Tsai, C.-S.; Chen, Y.-W.; Yeh, W.-K. Voltage-controlled multiple-valued logic design using negative differential resistance devices. *Solid State Electron.* **2010**, *54*, 1637–1640.
- (2) Ganjipour, B.; Dey, A. W.; Borg, B. M.; Ek, M.; Pistol, M.-E.; Dick, K. A.; Wernersson, L.-E.; Thelander, C. High current density Esaki tunnel diodes based on GaSb-InAsSb heterostructure nanowires. *Nano Lett.* **2011**, *11*, 4222–4226.
- (3) Desplanque, L.; Fahed, M.; Han, X.; Chinni, V. K.; Troadec, D.; Chauvat, M.-P.; Ruterana, P.; Wallart, X. Influence of nanoscale faceting on the tunneling properties of near broken gap InAs/AlGaSb heterojunctions grown by selective area epitaxy. *Nanotechnology* **2014**, *25*, 465302.
- (4) Özçelik, V. O.; Azadani, J. G. C.; Yang, S.; Koester, J.; Low, T. Band alignment of two-dimensional semiconductors for designing heterostructures with momentum space matching. *Phys. Rev. B: Condens. Matter Mater. Phys.* **2016**, *94*, 035125.
- (5) Hong, X.; Kim, J.; Shi, S.-F.; Zhang, Y.; Jin, C.; Sun, Y.; Tongay, S.; Wu, J.; Zhang, Y.; Wang, F. Ultrafast charge transfer in atomically thin MoS<sub>2</sub>/WS<sub>2</sub> heterostructures. *Nat. Nanotechnol.* **2014**, *9*, 682–686.
- (6) Özçelik, V. O.; Azadani, J. G.; Yang, C.; Koester, S. J.; Low, T. Band alignment of two-dimensional semiconductors for designing heterostructures with momentum space matching. *Phys. Rev. B: Condens. Matter Mater. Phys.* **2016**, *94*, 035125.
- (7) Tangi, M.; Mishra, P.; Ng, T. K.; Hedhili, M. N.; Janjua, B.; Alias, M. S.; Anjum, D. H.; Tseng, C.-C.; Shi, Y.; Joyce, H. J.; Li, L.-J.; Ooi, B. S. Determination of band offsets at GaN/single-layer MoS<sub>2</sub> heterojunction. *Appl. Phys. Lett.* **2016**, *109*, 032104.
- (8) Yan, X.; Liu, C.; Li, C.; Bao, W.; Ding, S.; Zhang, D. W.; Zhou, P. Tunable SnSe<sub>2</sub>/WSe<sub>2</sub> heterostructure tunneling field effect transistor. *Small* **2017**, *13*, 1701478.
- (9) Koswatta, S. O.; Koester, S. J.; Haensch, W. On the Possibility of Obtaining MOSFET-Like Performance and Sub-60-mV/dec Swing in 1-D Broken-Gap Tunnel Transistors. *IEEE Trans. Electron Devices* **2010**, *57*, 3222.
- (10) Tan, C.; Yin, S.; Chen, J. Broken-Gap PtS<sub>2</sub>/WSe<sub>2</sub> van der Waals Heterojunction with Ultrahigh Reverse Rectification and Fast Photoresponse. *ACS Nano* **2021**, *15*, 8328–8337.
- (11) Yang, Y.; Wang, Z. A two-dimensional MoS<sub>2</sub>/C<sub>3</sub>N broken-gap heterostructure, a first principles study. *RSC Adv.* **2019**, *9*, 19837.
- (12) Shim, J.; Kang, D.-H.; Kim, Y.; Kum, H.; Kong, W.; Bae, S.-H.; Almansouri, I.; Lee, K.; Park, J.-H.; Kim, J. Recent progress in Van der Waals heterojunction-based electronic and optoelectronic devices. *Carbon* **2018**, *133*, 78–89.
- (13) Shi, J.; Ou, Y.; Migliorato, M. A.; Wang, H.; Li, H.; Zhang, Y.; Gu, Y.; Zou, M. Tuning the electronic structure of GeC/WS<sub>2</sub> van der Waals heterostructure by electric field and strain: a first principles study. *Comput. Mater. Sci.* **2019**, *160*, 301–308.
- (14) Datta, S.; Das, B. Electronic Analog of the Electrooptic Modulator. *Appl. Phys. Lett.* **1990**, *56*, 665–667.
- (15) Nitta, J.; Akazaki, T.; Takayanagi, H.; Enoki, T. Spin-Orbit Interaction in an Inverted In<sub>0.53</sub>Ga<sub>0.47</sub>As/In<sub>0.52</sub>Al<sub>0.48</sub> As Heterostructure. *Phys. Rev. Lett.* **1997**, *78*, 1335–1338.
- (16) Schultz, M.; Heinrichs, F.; Merkt, U.; Colin, T.; Skauli, T.; Løvold, S. Rashba spin splitting in a gated HgTe quantum well. *Semicond. Sci. Technol.* **1996**, *11*, 1168–1172.
- (17) Engels, G.; Lange, J.; Schäpers, T.; Lüth, H. Experimental and theoretical approach to spin splitting in modulation-doped In<sub>x</sub>Ga<sub>1-x</sub>As/InP quantum wells for B→0. *Phys. Rev. B: Condens. Matter Mater. Phys.* **1997**, *55*, R1958–R1961.
- (18) Zeng, Z.; Yin, Z.; Huang, X.; Li, H.; He, Q.; Lu, G.; Boey, F.; Zhang, H. Single-layer semiconducting nanosheets: high-yield preparation and device fabrication. *Angew. Chem.* **2011**, *123*, 11289–11293.
- (19) Li, L.; Auer, E.; Liao, M.; Fang, X.; Zhai, T.; Gautam, U. K.; Lugstein, A.; Koide, Y.; Bando, Y.; Golberg, D. Deep-ultraviolet solar-blind photoconductivity of individual gallium oxide nanobelts. *Nanoscale* **2011**, *3*, 1120–1126.
- (20) Rasmussen, F. A.; Thygesen, K. S. Computational 2D materials database: electronic structure of transition-metal dichalcogenides and oxides. *J. Phys. Chem. C* **2015**, *119*, 13169–13183.
- (21) Qu, L.; Liu, Y.; Baek, J.-B.; Dai, L. Nitrogen-doped graphene as efficient metal-free electrocatalyst for oxygen reduction in fuel cells. *ACS Nano* **2010**, *4*, 1321–1326.
- (22) Wang, X.; Li, X.; Zhang, L.; Yoon, Y.; Weber, P. K.; Wang, H.; Guo, J.; Dai, H. N-doping of graphene through electrothermal reactions with ammonia. *Science* **2009**, *324*, 768–771.
- (23) Zhou, W.; Zou, X.; Najmaei, S.; Liu, Z.; Shi, Y.; Kong, J.; Lou, J.; Ajayan, P. M.; Yakobson, B. I.; Idrobo, J.-C. Intrinsic structural defects in monolayer molybdenum disulfide. *Nano Lett.* **2013**, *13*, 2615–2622.
- (24) Banhart, F.; Kotakoski, J.; Krasheninnikov, A. V. Structural defects in graphene. *ACS Nano* **2011**, *5*, 26–41.
- (25) Wu, W.; He, Q.; Jiang, C. Magnetic iron oxide nanoparticles: synthesis and surface functionalization strategies. *Nanoscale Res. Lett.* **2008**, *3*, 397–415.
- (26) Spinke, J.; Liley, M.; Schmitt, F. J.; Guder, H. J.; Angermaier, L.; Knoll, W. Molecular recognition at self-assembled monolayers: optimization of surface functionalization. *J. Chem. Phys.* **1993**, *99*, 7012–7019.
- (27) Geim, A. K.; Grigorieva, I. V. Van der Waals heterostructures. *Nature* **2013**, *499*, 419–425.
- (28) Liu, Y.; Weiss, N. O.; Duan, X.; Cheng, H.-C.; Huang, Y.; Duan, X. Van der Waals heterostructures and devices. *Nat. Rev. Mater.* **2016**, *1*, 16042.
- (29) Ruppert, C.; Aslan, O. B.; Heinz, T. F. Optical properties and band gap of single- and few-layer MoTe<sub>2</sub> crystals. *Nano Lett.* **2014**, *14*, 6231.
- (30) Lin, Y.-F.; Xu, Y.; Wang, S.-T.; Li, S.-L.; Yamamoto, M.; Aparecido-Ferreira, A.; Li, W.; Sun, H.; Nakaharai, S.; Jian, W.-B.; Ueno, K.; Tsukagoshi, K. Ambipolar MoTe<sub>2</sub> transistors and their applications in logic circuits. *Adv. Mater.* **2014**, *26*, 3263–3269.
- (31) Hamada, M.; Matsuura, K.; Sakamoto, T.; Muneta, I.; Hoshii, T.; Kakushima, K.; Tsutsui, K.; Wakabayashi, H. High hall-effect mobility of large-area atomic-layered polycrystalline ZrS<sub>2</sub> film using UHV RF magnetron sputtering and sulfurization. *IEEE J. Electron Devices Soc.* **2019**, *7*, 1258–1263.
- (32) Rehman, S. U.; Samad, A.; Saeed, M.; Amin, B.; Zhu, L. Computational insight of ZrS<sub>2</sub>/graphene heterobilayer as an efficient anode material. *Appl. Surf. Sci.* **2021**, *551*, 149304.
- (33) Zhang, L. M.; Zhang, W. B.; Qiao, S.; Yang, Y.; Shang, J. M.; Feng, S. Q. Two-dimensional ZrSe<sub>2</sub>/ZrS<sub>2</sub> heterobilayer tuned by electric field for optoelectronic devices. *J. Korean Phys. Soc.* **2022**, *80*, 606–612.
- (34) Zhang, K.; Zhang, T.; Cheng, G.; Li, T.; Wang, S.; Wei, W.; Zhou, X.; Yu, W.; Sun, Y.; Wang, P.; Zhang, D.; Zeng, C.; Wang, X.; Hu, W.; Fan, H. J.; Shen, G.; Chen, X.; Duan, X.; Chang, K.; Dai, N. Interlayer transition and infrared photodetection in atomically thin

- type-II MoTe<sub>2</sub>/MoS<sub>2</sub> van der Waals heterostructures. *ACS Nano* **2016**, *10*, 3852–3858.
- (35) Kresse, G.; Furthmüller, J. Efficient iterative schemes for ab initio total-energy calculations using a plane-wave basis set. *Phys. Rev. B: Condens. Matter Mater. Phys.* **1996**, *54*, 11169–11186.
- (36) Blöchl, P. E. Projector Augmented-Wave Method. *Phys. Rev. B: Condens. Matter Mater. Phys.* **1994**, *50*, 17953–17979.
- (37) Perdew, J. P.; Burke, K.; Ernzerhof, M. Generalized gradient approximation made simple. *Phys. Rev. Lett.* **1996**, *77*, 3865–3868.
- (38) Grimme, S. Semiempirical GGA-Type density functional constructed with a long-range dispersion correction. *J. Comput. Chem.* **2006**, *27*, 1787–1799.
- (39) Greenaway, D. L.; Nitsche, R. Preparation and optical properties of group IV–VI<sub>2</sub> chalcogenides having the CdI<sub>2</sub> structure. *J. Phys. Chem. Solids* **1965**, *26*, 1445–1458.
- (40) Ghafari, A.; Boochani, A.; Janowitz, C.; Manzke, R. Electronic structure of ZrS<sub>x</sub>Se<sub>2-x</sub> by Tran-Blaha modified Becke-Johnson density functional. *Phys. Rev. B: Condens. Matter Mater. Phys.* **2011**, *84*, 125205.
- (41) Wen, S.; Pan, H.; Zheng, Y. Electronic properties of tin dichalcogenide monolayers and effects of hydrogenation and tension. *J. Mater. Chem. C* **2015**, *3*, 3714–3721.
- (42) Grant, A. J.; Griffiths, T. M.; Pitt, G. D.; Yoffe, A. D. The electrical properties and the magnitude of the indirect gap in the semiconducting transition metal dichalcogenide layer crystals. *J. Phys. C: Solid State Phys.* **2001**, *8*, L17.
- (43) Zhou, J.; Lv, K.; Wang, Q.; Chen, X. S.; Sun, Q.; Jena, P. Electronic structures and bonding of graphene sheet and its BN analog. *J. Chem. Phys.* **2011**, *134*, 174701.
- (44) Tang, Z. K.; Zhang, Y. N.; Zhang, D. Y.; Lau, W. M.; Liu, L. M. The stability and electronic properties of novel three-dimensional graphene-MoS<sub>2</sub> hybrid structure. *Sci. Rep.* **2014**, *4*, 7007.
- (45) Ast, C. R.; Henk, J.; Ernst, A.; Moreschini, L.; Falub, M. C.; Pacilé, D.; Bruno, P.; Kern, K.; Grioni, M. Giant spin splitting through surface alloying. *Phys. Rev. Lett.* **2007**, *98*, 186807.
- (46) Sakamoto, K.; Kakuta, H.; Sugawara, K.; Miyamoto, K.; Kimura, A.; Kuzumaki, T.; Ueno, N.; Annese, E.; Fujii, J.; Kodama, A.; Shishidou, T.; Namatame, H.; Taniguchi, M.; Sato, T.; Takahashi, T.; Oguchi, T. Peculiar Rashba splitting originating from the two-dimensional symmetry of the surface. *Phys. Rev. Lett.* **2009**, *103*, 156801.
- (47) Lashell, S.; McDougall, B. A.; Jensen, E. Spin splitting of an Au (111) surface state band observed with angle resolved photoelectron spectroscopy. *Phys. Rev. Lett.* **1996**, *77*, 3419.
- (48) Koroteev, Y. M.; Bihlmayer, G.; Gayone, J. E.; Chulkov, E. V.; Blügel, S.; Echenique, P. M.; Hofmann, P. Strong spin-orbit splitting on Bi surfaces. *Phys. Rev. Lett.* **2004**, *93*, 046403.
- (49) Ke, C.; Wu, Y.; Zhou, J.; Wu, Z.; Zhang, C.; Li, X.; Kang, J. Modification of the electronic and spintronic properties of monolayer GaGeTe with a vertical electric field. *J. Phys. D: Appl. Phys.* **2019**, *52*, 115101.
- (50) Lu, A. K. A.; Houssa, M.; Luisier, M.; Pourtois, G. Impact of layer alignment on the behavior of MoS-ZrS<sub>2</sub> tunnel field-effect transistors: an ab initio study. *Appl. Phys. Rev.* **2017**, *8*, 034017.
- (51) Srivastava, P. K.; Hassan, Y.; Gebredingle, Y.; Jung, J.; Kang, B.; Yoo, W. J.; Singh, B.; Lee, C. Multifunctional van der Waals broken-gap heterojunction. *Small* **2019**, *15*, 1804885.

## □ Recommended by ACS

### A van der Waals Heterostructure with an Electronically Textured Moiré Pattern: PtSe<sub>2</sub>/PtTe<sub>2</sub>

Jingfeng Li, Matthias Batzill, et al.

MARCH 17, 2023

ACS NANO

READ ▶

### Superconductivity in Te-Deficient ZrTe<sub>2</sub>

Lucas E. Correa, Antonio J. S. Machado, et al.

MARCH 08, 2023

THE JOURNAL OF PHYSICAL CHEMISTRY C

READ ▶

### Valley Relaxation of the Moiré Excitons in a WSe<sub>2</sub>/MoSe<sub>2</sub> Heterobilayer

Keisuke Shinokita, Kazunari Matsuda, et al.

SEPTEMBER 28, 2022

ACS NANO

READ ▶

### Electron-Beam- and Thermal-Annealing-Induced Structural Transformations in Few-Layer MnPS<sub>3</sub>

Alexander Storm, Ute Kaiser, et al.

FEBRUARY 20, 2023

ACS NANO

READ ▶

Get More Suggestions >